RESEARCH ARTICLE | NOVEMBER 15 2023

Inverse design of graded phononic materials via ray tracing ⊘

Charles Dorn (ID) ; Dennis M. Kochmann ✉ (ID)

Check for updates

View Online   Export Citation   CrossMark

Inverse design of graded phononic materials via ray tracing

View Online   Export Citation   CrossMark

Charles Dorn [ID] and Dennis M. Kochmann[a) [ID]

AFFILIATIONS

Mechanics & Materials Lab, Department of Mechanical and Process Engineering, ETH Zürich, 8092 Zürich, Switzerland

[a)]Author to whom correspondence should be addressed: dmk@ethz.ch

ABSTRACT

We present a framework for the inverse design of spatially graded phononic materials based on ray tracing. Spatial grading of phononic materials allows the unit cell to vary smoothly in space. Compared to periodic architectures, spatial grading opens up a vast design space that promises new capabilities for manipulating elastic and acoustic waves. However, the use of spatial grading to control wave propagation has been limited to simple gradings, largely due to the bottleneck of modeling efficiency, and to the long-wavelength limit of low frequencies. In this work, ray tracing is exploited as an efficient alternative, around which we develop an optimization framework based on the adjoint state method toward the flexible inverse design of graded phononic materials. We demonstrate the design of graded mass-spring networks for objectives including focusing all directions of a point source, broadband focusing of a plane wave, and frequency sorting. These objectives are out of reach of periodic phononic materials, highlighting the high potential of spatially graded phononic materials. Moreover, our results demonstrate the importance of wave dispersion, which is classically neglected in the long-wavelength limit of elastodynamics.

I. INTRODUCTION

Periodic media exhibit remarkable dynamic properties including their ability to attenuate and guide waves. Phononic materials exploit periodic microstructure to control elastic and acoustic waves through the choice of the underlying unit cell.[1] Extensive research has focused on the design of phononic (meta-)materials with periodic architectures, aimed at optimizing a unit cell to have desirable wave propagation behavior (e.g., wide partial or full bandgaps).[2–4]

Compared to periodic architectures, spatially graded phononic materials (with unit cells that smoothly vary in space) have a considerably larger design space. As they locally resemble periodic media, graded architectures locally exhibit attenuation capabilities and extreme directionality, which allows for much richer wave manipulation than in periodic architectures. Despite this opportunity, significantly less work has focused on understanding and exploiting spatially graded phononic materials.

Past work exploring spatially graded phononic materials has been limited to restricted design spaces, such as linear grading,[5–7] analytical solutions (e.g., Luneburg lenses[8] and hyperbolic secant profiles[9,10]), and conformal mappings.[11] Within these restricted design spaces, fascinating wave physics has been demonstrated such as rainbow trapping,[12] wave focusing,[13] and low-pass wave attenuation.[11] However, the bottleneck of computation has prevented systematic exploration of the vast spatial grading design space for wave manipulation.

A major barrier to exploiting spatial grading is the computational expense of forward modeling. Periodic media benefit from Bloch wave analysis, allowing only single unit cell to be modeled, which does not directly apply to graded media. In the long-wavelength limit, homogenization admits the efficient modeling of (locally) periodic media as effective continua, which has driven an extensive literature of transformation-based design in acoustic and elastic metamaterials.[14–18] However, this body of work has been restricted to wave propagation in the long-wavelength limit. Beyond this homogenization limit, rich dispersive phenomena arise from waves interacting with the structure of the unit cells, which has remained widely unexplored. Direct numerical simulations (e.g., using finite element analysis) provide accurate models in this regime but are prohibitively inefficient for the inverse design since short length and time scales must be captured.

To fill this gap in modeling techniques, we previously developed ray theory in the context of spatially graded metamaterials,[19]

which generalized well-developed ray theories for "locally homogeneous" media[20] to the "locally periodic" setting, where dispersion due to the microstructure is captured. Based on local dispersion relations determined by the unit cell at a given location, ray tracing offers efficient approximate solutions for high-frequency/short-wavelength propagation (where the wavelength is assumed to be much shorter than the length scale of spatial grading).

Due to its efficiency and simplicity, ray tracing has been a workhorse for inverse problems in a wide range of fields from optical design[21,22] to seismic imaging[23] to x-ray tomography.[24] In this work, we develop ray-tracing-based inverse design in the new context of spatially graded phononic materials (in the dispersive, short-wavelength setting). We take inspiration from recent work on the optimal design of (non-dispersive) gradient-index optics,[25] which uses the adjoint state method to perform differentiable ray tracing and to enable gradient-based optimal design. In the dispersive setting, we derive a procedure for computing the gradient of a cost function that depends on ray trajectories. This provides a flexible setting for optimal phononic material design problems to be solved efficiently.

Using this inverse design framework, we explore the interesting physics enabled by an arbitrary spatial grading of phononic materials. To represent a generic phononic material, we investigate a two-dimensional (2D) mass-spring network with spatially graded mass and spring stiffness. Through our optimization framework, we demonstrate extensive control over wave propagation. As an example, grading can be designed to focus nearly all directions of a wave emanating from a point source at a desired location. Broadband focusing of a plane wave as well as sorting frequencies of a plane wave to different locations are also demonstrated. Overall, the proposed methodology enables exploring the vast design space of graded phononic materials and the intriguing wave phenomena it offers.

II. FORWARD MODELING

We begin by briefly reviewing the method of ray tracing to solve the forward problem of how a wave propagates in a given graded phononic material. Additionally, we present an example of forward modeling based on ray tracing in the context of a graded mass-spring network.

A. Ray tracing in phononic materials

The underlying approximation is *local periodicity*: if the grading is sufficiently slow, the material is nearly periodic in the local neighborhood of each unit cell, so it is assumed that the local dispersion relations are valid in that neighborhood. The medium is consequently treated as a continuum described at each point by its local dispersion relations. The local dispersion relations of a particular unit cell are obtained from Bloch wave analysis, as if that unit cell belonged to an infinite periodic lattice. Thus, the local dispersion relation takes the form $\omega = \omega(\boldsymbol{k}, \boldsymbol{x})$, relating the eigenfrequency ω to the wave vector $\boldsymbol{k} \in \mathbb{R}^d$ at a given spatial location $\boldsymbol{x} \in \mathbb{R}^d$ (where d is the spatial dimension).

We consider *dispersive* wave propagation, where the group velocity $\boldsymbol{v} = \frac{\partial \omega}{\partial \boldsymbol{k}}$ varies with frequency. In contrast, waves are

non-dispersive when the group velocity equals the phase velocity $\boldsymbol{v}_p = \frac{\omega}{k} \hat{\boldsymbol{k}}$ (where k and $\hat{\boldsymbol{k}}$ are, respectively, the magnitude and direction of the wave vector), which occurs in the low-frequency limit.

Given the local dispersion relations, wave propagation is efficiently modeled by ray tracing. The ray tracing equations, which are a system of first-order ordinary differential equations, take the form

$$\dot{\boldsymbol{x}} = \frac{\partial \omega}{\partial \boldsymbol{k}}, \tag{1}$$

$$\dot{\boldsymbol{k}} = -\frac{\partial \omega}{\partial \boldsymbol{x}}, \tag{2}$$

where dots denote derivatives with respect to time t of the ray trajectory $\boldsymbol{x}(t)$ and the wave vector $\boldsymbol{k}(t)$ along the ray. Equation (1) states that the group velocity is tangent to the ray trajectory, while Eq. (2) states that the wave vector evolves along the ray due to the spatial variation in the local dispersion relations. Given initial conditions $\boldsymbol{x}_0 = \boldsymbol{x}(t = 0)$ and $\boldsymbol{k}_0 = \boldsymbol{k}(t = 0)$, the ray tracing system can be solved as an initial value problem, providing an efficient solution to the forward problem.

For a general derivation of ray theory for linear elastic waves in locally periodic media, see Ref. 19 (which also extends to acoustic waves as a special case of elasticity).

B. Mass-spring network example

As a prototypical phononic material, we study an infinite 2D mass-spring network throughout this paper. The mass-spring network consists of a 2D square grid of masses m connected by linear elastic springs in the horizontal and vertical directions with stiffness K_x and K_y, respectively, as shown in Fig. 1. The spacing
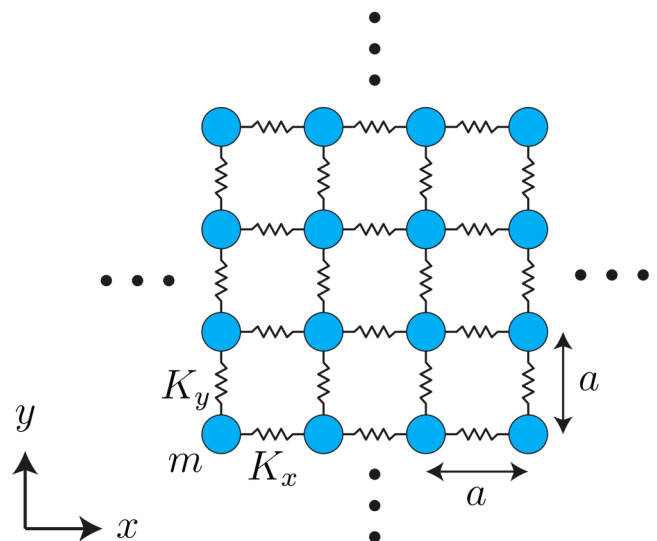

FIG. 1. Mass-spring network in 2D (particles of identical mass m are connected by elastic springs of stiffness K_x and K_y).

between masses in the horizontal and vertical directions is a. Each mass has only one degree of freedom, the out-of-plane displacement u, and the spring forces are proportional to the relative out-of-plane displacements of adjacent masses. This mass-spring network provides a simple setting that is commonly used for understanding waves in 2D phononic media.[1,26]

The equation of motion of the mass at point (i,j) takes the form

$$m\ddot{u}_{i,j} + 2(K_x + K_y)u_{i,j} - K_x\big(u_{i-1,j} + u_{i+1,j}\big) \\ - K_y\big(u_{i,j-1} + u_{i,j+1}\big) = 0. \tag{3}$$

For a periodic network, a unit cell consists of a single mass, and the corresponding dispersion relation follows as:[1]

$$\omega = \sqrt{\frac{2}{m}}\Big[K_x + K_y - K_x\cos(ak_x) - K_y\cos(ak_y)\Big]^{\frac{1}{2}}, \tag{4}$$

where k_x and k_y are, respectively, the x- and y-components of the wave vector. For a graded network (with spatially varying mass or stiffness values), (4) represents the local dispersion relation when evaluated with the local unit cell's properties.

To exemplify ray tracing for the forward modeling of wave propagation, we consider spatial grading of the mass m. An arbitrary spatial grading of mass is taken to be $m = 0.5m_0\sin(0.1x/a + 0.05y/a) + m_0$. The stiffness of all springs is taken as $K_x = K_y = K_0$. A harmonic displacement excitation of frequency $\omega_f = 1.75\omega_0$ and magnitude $\hat{u}$ is applied to the mass at the origin, where the frequency is normalized by $\omega_0 = \sqrt{K_0/m_0}$. Figure 2(a) shows the local dispersion at the excitation location.

To model the wave emanating from the point source, ray tracing is performed by solving Eqs. (1) and (2). The initial position $\boldsymbol{x}_0$ of each ray is the location of the point source, here the origin. The initial wave vector $\boldsymbol{k}_0$ must lie on the $\omega_f = 1.75/\omega_0$ level set of the dispersion surface at the excitation location, which

is highlighted in Fig. 2(a). To capture waves propagating in all directions from the point source, 100 rays are traced with initial wave vectors densely sampling the excitation frequency level set. The resulting ray trajectories until time $t = 47/\omega_0$ are plotted in Fig. 2(b).

As a reference, a transient simulation is performed by numerically solving the equation of motion, Eq. (3), on a finite domain. A harmonic displacement excitation at frequency ω_f is applied at the origin, and the domain is chosen sufficiently large such that the wave does not reach the boundary by $t = 47/\omega_0$, when the simulation is stopped. Figure 2(c) shows the thus-obtained maximum displacement amplitude throughout the mass-spring network during the simulation. The ray trajectories of Fig. 2(b) clearly align with the regions of high amplitude in Fig. 2(c). Thus, ray tracing provides an accurate and efficient method for modeling wave propagation in this graded phononic material.

It is also possible to compute displacement amplitudes along each ray in the forward modeling process.[19] However, accounting for ray amplitudes in inverse problems (which has been well studied in seismology[27]) adds significant complexity, which is why we restrict this paper to considering ray trajectories only.

III. INVERSE DESIGN FRAMEWORK

We aim to solve the inverse problem of designing a phononic material that achieves desired wave propagation behavior (e.g., focusing a wave at a prescribed point). This inverse design challenge is formulated as an optimization problem, whose cost function requires evaluating the forward problem. Ray tracing provides an efficient and differentiable means of solving the forward problem. To enable gradient-based optimization, we obtain the cost function gradient using the adjoint state method.

While the focus of this study is on phononic materials, we formulate the inverse design framework in terms of an arbitrary dispersion relation. Thus, it applies generally to the wide range of fields where ray theory is valid.
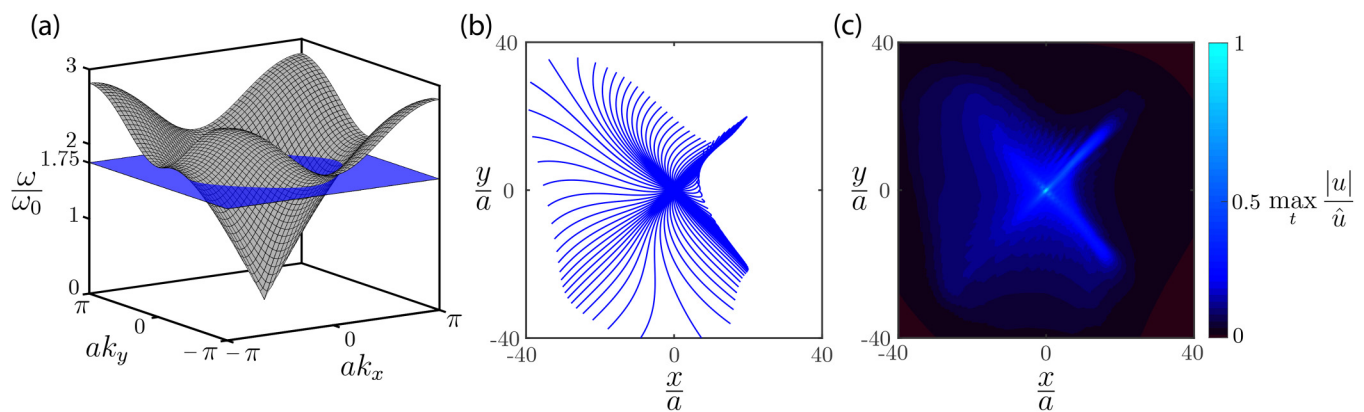
FIG. 2. Example of forward modeling of wave propagation in a graded mass-spring network. (a) Local dispersion relation at the excitation location with the plane corresponding to the excitation frequency $\omega_f = 1.75\omega_0$ highlighted. (b) Ray trajectories at time $t = 47/\omega_0$. (c) Maximum displacement amplitude in a transient simulation of a finite mass-spring network.

A. Problem definition

Using ray tracing as a basis for the inverse design problem, we seek to prescribe the behavior of ray trajectories. Specifically, we pursue solutions where the trajectory of ray r, which starts at point $\boldsymbol{x}_{0r}$, passes through a prescribed point $\hat{\boldsymbol{x}}_r$. This objective can be achieved by minimizing a cost function for ray r of the form $c_r = (\varphi_r^* - \hat{\varphi})^2$, where $\hat{R}$ and $\hat{\varphi}$ are the polar coordinates of $\hat{x}$ with respect to $\boldsymbol{x}_{0r}$ (see Fig. 3). Point $\boldsymbol{x}_r^*$ is defined as the point at which ray r reaches a distance of $\hat{R}$ from point $\boldsymbol{x}_{0r}$, and the angular coordinate of $\boldsymbol{x}_r^*$ with respect to $\boldsymbol{x}_0$ is denoted φ_r^*. The time t_r^* is the time at which the ray reaches the distance $\hat{R}$ from its starting point, such that $\boldsymbol{x}_r^* = \boldsymbol{x}_r(t^*)$. Figure 3 illustrates this objective for two rays i and j.

To achieve a solution that minimizes the cost function, we pose an optimization problem over a set of design variables that are summarized in a vector $\boldsymbol{\theta} \in \mathbb{R}^N$. The design variables contain N material or geometric parameters of unit cells. In the context of the mass-spring network of Fig. 1, $\boldsymbol{\theta}$ could contain, e.g., K_x, K_y, and m of individual unit cells.

The inverse design problem is cast as an optimization problem of the form

$$
\begin{aligned}
\min_{\boldsymbol{\theta}} \; & C(\boldsymbol{\theta}) & \text{subject to} \\
& \dot{\boldsymbol{x}}_r = \frac{\partial \omega}{\partial \boldsymbol{k}}, & t \in [0, t_r^*], \; r = 1, \ldots, n_r, \\
& \dot{\boldsymbol{k}}_r = -\frac{\partial \omega}{\partial \boldsymbol{x}}, & t \in [0, t_r^*], \; r = 1, \ldots, n_r, \\
& \mathscr{G}_r(\boldsymbol{x}_r^*) = 0, & r = 1, \ldots, n_r,
\end{aligned}
\tag{5}
$$

where the overall cost function C is the sum of functions c_r
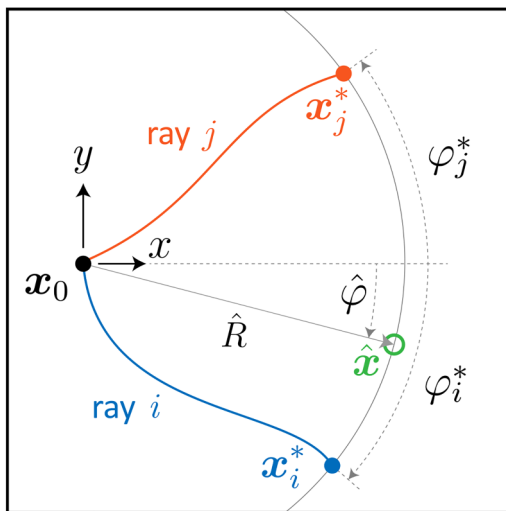
FIG. 3. The cost functions for rays i and j are $c_i = (\varphi_i^* - \hat{\varphi})^2$ and $c_j = (\varphi_j^* - \hat{\varphi})^2$, respectively. Minimizing the cost function aims to steer each ray, emanating from $\boldsymbol{x}_0$, through the prescribed point $\hat{x}$ at a distance $\hat{R}$.

associated with the individual rays,

$$
C(\boldsymbol{\theta}) = \sum_{r=1}^{n_r} c_r(\boldsymbol{x}_r^*(\boldsymbol{\theta})),
\tag{6}
$$

and n_r is the number of rays. Each ray's cost function depends on $\boldsymbol{\theta}$ only through the trajectory of ray r at time t^*, denoted $\boldsymbol{x}_r^*(\boldsymbol{\theta}) = \boldsymbol{x}_r(\boldsymbol{\theta}, t^*)$. The ray tracing Eqs. (1) and (2) are treated as constraints, enforcing that the ray trajectories are solutions to the forward problem.

The last constraint in Eq. (5) arises because the end time t_r^* depends on the design variables. Specifically, we take $\mathscr{G}_r$ as the signed distance function from the ray r to the circle centered at $\boldsymbol{x}_0$ with radius $\hat{R}$, so that $\mathscr{G}_r = 0$ enforces that time t_r^* corresponds to when ray r passes through this circle. (Alternatively, one could prescribe t^* for each ray and omit the third constraint, which leads to a more restrictive design problem).

To solve this optimization problem using gradient-based algorithms, the total derivative of the cost function with respect to the design variables, $\frac{dC}{d\boldsymbol{\theta}}$, is required. Obtaining this derivative is challenging since it is not explicitly available. That is, computing it through the chain rule requires $\frac{d\boldsymbol{x}^*}{d\boldsymbol{\theta}}$ (the sensitivity of a ray's trajectory due to a design perturbation), which cannot be obtained analytically. Of course, finite difference schemes are capable of approximating $\frac{d\boldsymbol{x}^*}{d\boldsymbol{\theta}}$, but become prohibitively expensive to compute if there are many design variables, which is the case for the problems we address. To efficiently compute the cost function gradient, we employ the adjoint state method.

B. The adjoint state method

The adjoint state method is a general approach for computing gradients for optimization problems constrained by differential equations.[28] For decades, it has been a useful tool for solving inverse problems,[29] with applications in a range of fields including seismology,[30] optics,[31] and control systems.[32] Recently, it was developed for the inverse design of (non-dispersive) gradient-index optics in the context of ray tracing.[25] Here, we generalize the formulation of Teh *et al.*[25] to apply to dispersive waves. For clarity, we formulate this section and the following Sec. III C for an individual ray and omit subscripts to identify a particular ray.

The adjoint state method relies on Lagrange multipliers to compute the cost function gradient. Let $\boldsymbol{\lambda} \in \mathbb{R}^d$ and $\boldsymbol{\mu} \in \mathbb{R}^d$ be the Lagrange multipliers associated with Eqs. (1) and (2), respectively. Thus, $\boldsymbol{\lambda}$ and $\boldsymbol{\mu}$ are time-dependent, varying along a ray. In addition, the Lagrange multiplier ρ is introduced to enforce the third constraint of Eq. (5). We define the vector $\boldsymbol{p}(\boldsymbol{\theta}, t)$ containing the state variables $\boldsymbol{x}$ and $\boldsymbol{k}$, and the vector $\boldsymbol{\Lambda}(\boldsymbol{\theta}, t)$ containing the Lagrange multipliers $\boldsymbol{\lambda}$ and $\boldsymbol{\mu}$ as

$$
\boldsymbol{p} = \begin{bmatrix} \boldsymbol{x} \\ \boldsymbol{k} \end{bmatrix}, \quad \boldsymbol{\Lambda} = \begin{bmatrix} \boldsymbol{\lambda} \\ \boldsymbol{\mu} \end{bmatrix}.
\tag{7}
$$

The Lagrangian takes the form

$$\mathscr{L}\left(\boldsymbol{\theta}, \boldsymbol{p}, \boldsymbol{\Lambda}, \rho, t^*\right) = C - \int_0^{t^*} \boldsymbol{\Lambda}^T \boldsymbol{S} \, dt - \rho \mathscr{G}, \quad (8)$$

where

$$\boldsymbol{S} = \begin{bmatrix} \dot{\boldsymbol{x}} - \frac{\partial \omega}{\partial \boldsymbol{k}} \\ \dot{\boldsymbol{k}} + \frac{\partial \omega}{\partial \boldsymbol{x}} \end{bmatrix}. \quad (9)$$

Note that the variables $\boldsymbol{p}$, $\boldsymbol{\Lambda}$, ρ, and t^* all depend on $\boldsymbol{\theta}$.

The adjoint state method proceeds by requiring stationarity with respect to all variables except $\boldsymbol{\theta}$. Enforcing stationarity with respect to $\boldsymbol{\Lambda}$ returns the ray tracing equations $\boldsymbol{S} = \boldsymbol{0}$, requiring $\boldsymbol{p}$ to trace a ray. Stationarity with respect to ρ enforces the constraint $\mathscr{G} = 0$, which defines the ray's end time t^*. The *adjoint equation* follows from stationarity with respect to $\boldsymbol{p}$ as

$$\delta_{\boldsymbol{p}} \mathscr{L} = \frac{\partial C}{\partial \boldsymbol{p}^*} \delta \boldsymbol{p}^* - \int_0^{t^*} \boldsymbol{\Lambda}^T \frac{\partial \boldsymbol{S}}{\partial \boldsymbol{p}} \delta \boldsymbol{p} \, dt - \rho \frac{\partial \mathscr{G}}{\partial \boldsymbol{p}} \delta \boldsymbol{p} = 0. \quad (10)$$

This is used to solve for the Lagrange multipliers $\boldsymbol{\Lambda}$, which will be discussed in Sec. III C. Finally, stationarity with respect to t^* yields

$$\frac{d\mathscr{L}}{dt^*} = \frac{\partial C}{\partial \boldsymbol{x}^*} \frac{\partial \boldsymbol{x}^*}{\partial t} - \left[\boldsymbol{\Lambda}^T \boldsymbol{S} \right]_{t^*} - \rho \frac{\partial \mathscr{G}}{\partial \boldsymbol{x}^*} \frac{\partial \boldsymbol{x}^*}{\partial t} = 0. \quad (11)$$

Denoting $\boldsymbol{v}^*$ as the group velocity at time t^* and noting that $\boldsymbol{S} = \boldsymbol{0}$, Eq. (11) is solved for ρ to obtain

$$\rho = \frac{\frac{\partial C}{\partial \boldsymbol{x}} \cdot \boldsymbol{v}^*}{\frac{\partial \mathscr{G}}{\partial \boldsymbol{x}} \cdot \boldsymbol{v}^*}. \quad (12)$$

The quantity $\frac{\partial \mathscr{G}}{\partial \boldsymbol{x}^*}$ is the normal vector to the circle of radius $\hat{R}$ centered at $\boldsymbol{x}_0$.[25]

After enforcing stationarity with respect to $\boldsymbol{\Lambda}$ and ρ (which enforce the constraints) as well as $\boldsymbol{p}$ and t^* (which determine the Lagrange multipliers), the gradient of the cost function with respect to $\boldsymbol{\theta}$ is easily obtained. Since $\boldsymbol{S}(\boldsymbol{p}, \boldsymbol{\theta})$ and $\mathscr{G}(\boldsymbol{p})$ are zero everywhere, and, therefore, $\frac{d\boldsymbol{S}}{d\boldsymbol{\theta}}$ and $\frac{d\mathscr{G}}{d\boldsymbol{\theta}}$ vanish, it follows that

$$\frac{dC}{d\boldsymbol{\theta}} = \frac{\delta \mathscr{L}}{\delta \boldsymbol{\theta}}. \quad (13)$$

Since the variations of the Lagrangian with respect to all variables except $\boldsymbol{\theta}$ are zero, only one term of $\frac{\delta \mathscr{L}}{\delta \boldsymbol{\theta}}$ survives, which gives

$$\frac{dC}{d\boldsymbol{\theta}} = - \int_0^{t^*} \boldsymbol{\Lambda}^T \frac{\partial \boldsymbol{S}}{\partial \boldsymbol{\theta}} \, dt. \quad (14)$$

Here, the utility of the adjoint state method becomes evident. It enables the computation of $\frac{dC}{d\boldsymbol{\theta}}$ without knowledge of $\frac{d\boldsymbol{p}}{d\boldsymbol{\theta}}$, instead using the more easily obtained Lagrange multipliers $\boldsymbol{\Lambda}$. A procedure for computing $\boldsymbol{\Lambda}$ and the cost function gradient is presented in Sec. III C.

C. Gradient computation procedure

In our examples, we define a total of D (material or geometric) design parameters describing a unit cell, whose spatial distribution is to be optimized on a regular square $n \times n$ grid containing n^2 points, with spacing Δ. Vector $\boldsymbol{\theta}^{(i)} \in \mathbb{R}^{n^2}$ (where $i = 1, \ldots, D$) contains the values of the ith design parameter at each of the n^2 grid points. The vector containing all design parameters at all grid points is $\boldsymbol{\theta} \in \mathbb{R}^N$ with $N = n^2 D$, which takes the form

$$\boldsymbol{\theta} = \begin{bmatrix} \vdots \\ \boldsymbol{\theta}^{(i)} \\ \vdots \end{bmatrix}. \quad (15)$$

For example, in the mass-spring network examples of Fig. 1, $\boldsymbol{\theta}^{(1)}$ contains the horizontal and $\boldsymbol{\theta}^{(2)}$ the vertical spring stiffness values, while $\boldsymbol{\theta}^{(3)}$ contains the masses, evaluated on a uniform grid and resulting in a spatially graded lattice, as shown in Fig. 4. This setup forms the basis for the examples presented in Sec. IV.

Computing the cost function derivative with respect to the design variables involves three steps. First, the forward ray tracing problem is solved to compute ray trajectories. Then, the adjoint equation is solved by tracing backward along the ray to obtain the Lagrange multipliers. With the ray trajectory and Lagrange multipliers in hand, Eq. (14) is evaluated to obtain the cost function gradient. These steps are illustrated in Fig. 4 for a single ray.

The first step of forward ray tracing is straightforward, as it involves numerically solving Eqs. (1) and (2) for some initial conditions $\boldsymbol{x}_0$ and $\boldsymbol{k}_0$. Initial conditions of the ray depend on the problem one aims to solve and remain unchanged throughout the optimization.

The second step of backward tracing involves numerically solving a system of first-order differential equations that arises from the adjoint state equation. In Appendix A, we show that the adjoint state equation of Eq. (10) is equivalent to the following system:

$$\dot{\boldsymbol{\lambda}} = - \frac{\partial^2 \omega}{\partial \boldsymbol{x} \partial \boldsymbol{k}} \boldsymbol{\lambda} + \frac{\partial^2 \omega}{\partial \boldsymbol{x} \partial \boldsymbol{x}} \boldsymbol{\mu}, \quad (16)$$

$$\dot{\boldsymbol{\mu}} = - \frac{\partial^2 \omega}{\partial \boldsymbol{k} \partial \boldsymbol{k}} \boldsymbol{\lambda} + \frac{\partial^2 \omega}{\partial \boldsymbol{k} \partial \boldsymbol{x}} \boldsymbol{\mu}, \quad (17)$$

with end conditions at $t = t^*$ given by

$$\boldsymbol{\lambda}(t^*) = \frac{\partial C}{\partial \boldsymbol{x}^*} - \rho \frac{\partial \mathscr{G}}{\partial \boldsymbol{x}^*}, \quad (18)$$

$$\boldsymbol{\mu}(t^*) = \boldsymbol{0}. \quad (19)$$

This system can be solved backward along the ray, starting from the end conditions at t^* and marching toward $t = 0$ [where ρ is known from Eq. (12)].
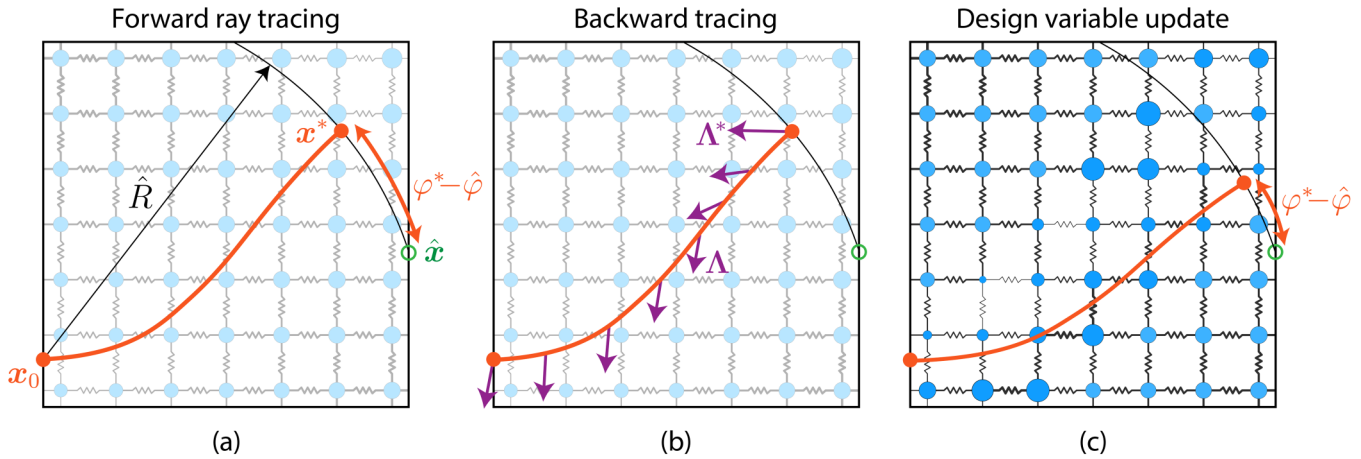
FIG. 4. Inverse design procedure. (a) Step 1: forward ray tracing. (b) Step 2: backward tracing to compute the Lagrange multipliers Λ along the ray. (c) Step 3: update design variables surrounding the ray path using the cost function gradient.

The final step is to evaluate the gradient of the design variables. Equation (14) can be rewritten as

$$\frac{dC}{d\boldsymbol{\theta}} = -\int_0^{t^*} \left(-\boldsymbol{\lambda}^\top \frac{\partial^2 \omega}{\partial \boldsymbol{k} \partial \boldsymbol{\theta}} + \boldsymbol{\mu}^\top \frac{\partial^2 \omega}{\partial \boldsymbol{x} \partial \boldsymbol{\theta}} \right) dt. \qquad (20)$$

Once the ray trajectory and Lagrange multipliers are known, this can be evaluated along each ray to compute the cost function gradient.

To evaluate the (first and second) derivatives of the dispersion relations that appear in Eqs. (1), (2), (16), (17), and (20), an interpolation scheme is used. Appendix B outlines the computation of the required dispersion relation derivatives based on the interpolated design parameters.

This three-step procedure is illustrated in Fig. 4 for a single ray. The first step [Fig. 4(a)] represents the forward problem of computing ray trajectories $\boldsymbol{x}$ for a given design by solving Eqs. (1) and (2). The second step [Fig. 4(b)] involves solving the adjoint system of Eqs. (16) and (17) backward along the ray to obtain the Lagrange multipliers. Once the Lagrange multipliers are known, the gradient of the cost function is computed by integrating Eq. (20) along the ray, which is used to update the design variables [Fig. 4(c)] through a standard gradient-based nonlinear optimization scheme. After updating the design variables, the ray is closer to satisfying the objective function. This procedure is iteratively repeated, until convergence is achieved, which is defined as when the sum of each ray's cost function becomes smaller than a tolerance ε (we used $\varepsilon = 10^{-4}$ in our examples).

Since ray tracing in phononic materials relies on the assumption of local periodicity, and, therefore, of slow spatial grading (relative to wavelengths of interest), we use regularization to penalize large spatial derivatives of design parameters. Specifically, we augment the cost function by a term penalizing the total variation of each design parameter $\boldsymbol{\theta}^{(i)}$, replacing Eq. (6) by

$$C(\boldsymbol{\theta}) = \sum_r c_r(\boldsymbol{x}_r^*(\boldsymbol{\theta}))$$
$$+ \kappa \sum_i \sum_{j,k} \sqrt{(\theta_{j,k}^{(i)} - \theta_{j+1,k}^{(i)})^2 + (\theta_{j,k}^{(i)} - \theta_{j,k-1}^{(i)})^2} \Delta^2, \qquad (21)$$

where $\theta_{j,k}^{(i)}$ is the design parameter evaluated at grid point (j, k) and κ is a scalar controlling the strength of the regularization term. The regularization term does not affect the adjoint state formulation, and the gradient of the regularization term can be directly added to Eq. (20).

To solve the optimization problem given the cost function gradient, many algorithms are available and the best performing algorithm may be problem-dependent. We found a quasi-Newton optimizer, specifically the L-BFGS algorithm[33] using the NLopt implementation,[34] to perform well. To solve the ray tracing and backward tracing systems, a third-order Runge–Kutta scheme was used with a fixed step size to ensure that backward tracing follows the same steps as forward tracing. A variable-resolution implementation was used, similar to the methodology of Teh et al.,[25] which involves beginning the optimization on a spatially coarse grid of design parameters and refining the grid as the optimization progresses. Starting the optimization on a coarse grid (e.g., a design variable grid spacing of 16 unit cells, such that $\Delta = 16a$) both encourages a smooth solution and boosts efficiency compared to initializing the optimization on a fine grid (a design variable grid spacing of one unit cell, such that $\Delta = a$).

IV. RESULTS

We demonstrate this inverse design framework in the context of the mass-spring network of Fig. 1. Three design parameters are considered: K_x, K_y, and m. In the following examples, we design

the spatial distributions of these design variables to optimize a given cost function. Three examples are presented, which achieve focusing of a point source, broadband focusing of a plane wave, and frequency sorting. Optimal designs are validated by comparison to transient numerical simulations.

A. Point source focusing

For the first example, we design the mass-spring network to focus the entire wave emerging from a harmonic point source to a specified focal point. The point source is located at the origin and the target focal point has coordinates $\hat{\boldsymbol{x}} = (60a, 0)^T$.

To achieve focusing, we define the cost function as

$$c_r = \varphi_r^{*2}. \tag{22}$$

The time t_r^* is defined as the time at which ray r crosses a circle with radius $\hat{R} = 60a$. Minimizing the cost function drives all considered rays emerging from the point source to cross through the focal point. At the point source, the mass and stiffness are fixed at $m = m_0$ and $K_x = K_y = K_0$ to ensure that the initial conditions of the rays do not change throughout the optimization. The mass and stiffness of all unit cells on an 160×160 grid are taken as design variables, which leads to a total of $76\,800$ design variables.

The frequency of the harmonic point source is taken to be $1.25\omega_0$ as an example, where $\omega_0 = \sqrt{K_0/m_0}$. Figure 5(d) plots the local dispersion relation at the excitation location with the excitation frequency highlighted. Initial conditions for the wave vector of the rays emerging from the point source lie on the isofrequency contour of the dispersion relations at $\omega = 1.25\omega_0$. We take 84 rays uniformly spanning all initial directions from the point source, except directions within $\pm 7°$ from the x-axis (nearly horizontal directions were found to be numerically problematic, see Sec. IV D).

To ensure reasonable values for the design variables, the normalized design variables K_x/K_0, K_y/K_0, and m/m_0 are restricted to a lower bound of 0.2 and an upper bound of 2 during the optimization. As the initial guess for the optimization, all mass and stiffness values are taken as $K_x = K_y = K_0$ and $m = m_0$. Based on numerical experiments, the regularization constant was taken as $\kappa = 0.001$. An analysis of the trade-off between the ray term and the regularization term in the cost function was not performed, since the chosen value of κ was found to lead to a global minimization of the ray term (i.e., $\sum c_r < \varepsilon$).

The output of the optimization is a spatial distribution of the design variables, which is plotted in Figs. 5(a)–5(c). Interestingly, the solution exhibits spatial grading in two design variables, leaving K_x nearly uniform. However, the solution is not necessarily unique; this is a non-convex optimization problem and other solutions may
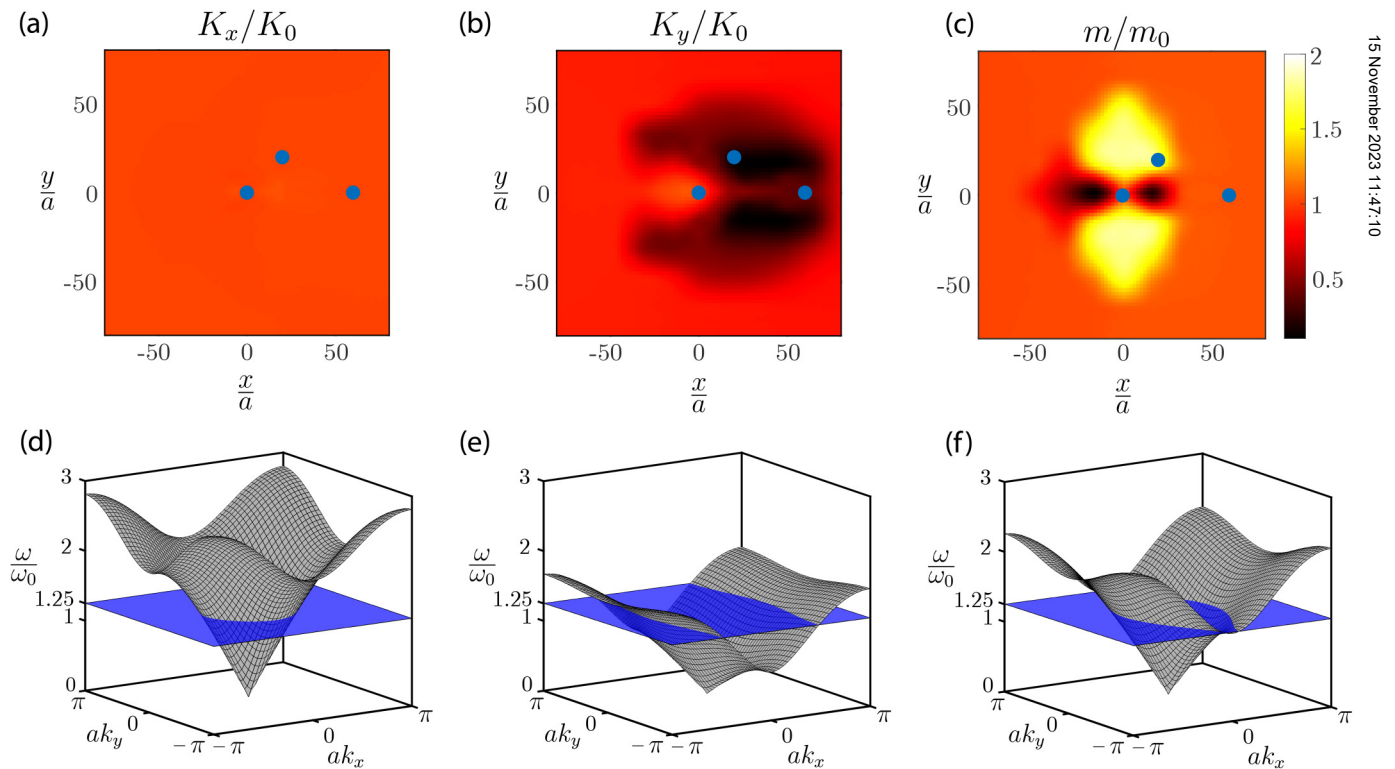
FIG. 5. Point source focusing example. Optimal spatial distributions of (a) K_x, (b) K_y, and (c) m. Local dispersion relation at (d) the excitation point (0,0), (e) the point (20a, 20a), and (f) the focal point (60a, 0), where the design frequency is highlighted by the blue planes. These three points are marked with dots in (a)–(c).

exist with different design variable distributions. To highlight the variation in local dispersion relations throughout the optimally graded lattice, Figs. 5(e) and 5(f) show the local dispersion surface at the point $(x, y) = (20a, 20a)$ and the focal point, respectively. In the optimal design, the forcing frequency level set ranges from being near the low-frequency limit [Fig. 5(d)] to near the top of the dispersion surface [Fig. 5(e)]—clearly showing that wave dispersion must be accounted for.

Ray trajectories corresponding to the optimal design variables are shown in Fig. 6(a), which all start at the excitation point and pass through the target focal point. The ray trajectories in Fig. 6(a) are plotted only until they reach the focal point, though the specific time at which each ray passes through the focal point is not the same for all rays. For clarity, only one third of the rays are shown in Fig. 6(c).

A transient numerical simulation was performed to validate the optimal solution. The equations of motion, Eq. (3), were solved numerically on a finite domain with the optimal mass and stiffness distributions of Figs. 5(a)–5(c). A harmonic displacement excitation of amplitude $\hat{u}$ and frequency $\omega = 1.25\omega_0$ was applied to the mass at the origin. The simulation was stopped at time $t = 165/\omega_0$, and the simulated domain was sufficiently large so that boundary effects were avoided. In Fig. 6(b), the maximum displacement of each mass during the simulation is plotted. It is evident that the ray paths correspond to the regions of high amplitude in the transient simulation. A sharp peak in displacement amplitude is observed at the mass located at the target focal point $\hat{x}$, which exhibits the largest displacement amplitude in the entire domain. The maximum displacement amplitude observed at $\hat{x}$ is $u = 1.08\hat{u}$, which is higher than the amplitude $\hat{u}$ at the point source, confirming that a strong focusing effect is achieved. An animation of the transient simulation is included in Supplementary Video 1.

B. Broadband plane wave focusing

For the next example, the mass and stiffness distributions are designed for broadband focusing of an incident plane wave. We consider a line source along the y-axis from $y = -10a$ to $y = 10a$, which generates a plane wave that we aim to focus at the point $\hat{x} = (50a, 50a)^T$ [see Fig. 7(c)]. To achieve broadband focusing, five design frequencies are included in the optimization: $\omega_1 = \omega_0$, $\omega_2 = 1.125\omega_0$, $\omega_3 = 1.25\omega_0$, $\omega_4 = 1.375\omega_0$, and $\omega_5 = 1.5\omega_0$. The local dispersion relation at the line source is shown in Fig. 7(a) with the excitation frequencies highlighted. The cost function again takes the form of Eq. (22) to steer all rays through $\hat{x}$, where x^* is the ray position at time t^*, when the ray crosses a radius of $\hat{R}$. Unlike in the previous example, $\hat{R}$ is different for each ray in this example since each ray starts at a different location.

In the region $x \leq 0$, the mass and stiffness values are fixed at $K_x = K_y = K_0$ and $m = m_0$ to ensure the initial conditions of the rays are unchanged throughout the optimization. An initial guess of uniform mass and stiffness is again used. Twenty rays of each frequency are taken in the cost function, which have evenly spaced initial positions from $y = -10a$ to $y = 10a$. The initial wave vector for a ray of frequency ω_r is determined as the point on the ω_r iso-frequency contour with group velocity in the positive x-direction. The regularization constant is taken as $\kappa = 0.0001$, which is different from the previous example, as we found that an appropriate regularization constant that leads to global minimization of the ray term of the cost function is problem-dependent.

Figure 7(b) shows the optimal design variable distributions, whose values range from 0.58 to 1.34 (the same bounds on the normalized design variables, from 0.2 to 2, are applied in the optimization, but the optimal solution did not reach the bounds). The corresponding optimal ray trajectories are plotted in Fig. 7(c). While all considered rays pass through the focal point, rays with different frequencies (but the same initial position) take different paths to the focal point.

A transient numerical solution was performed to validate the design. To approximate an incident plane wave, the line source was applied by prescribing a harmonic displacement along the y-axis. Displacements of the form $u(y, t) = A(y) \sum_{i=1}^5 \sin(\omega_i t)$ were applied. To ensure that most energy emanates from the region between $y = -10a$ and $y = 10a$ while minimizing edge effects, a Gaussian amplitude profile $A(y)$ was prescribed, centered at $y = 0$ where the amplitude is $\hat{u}$, with a standard deviation of $4a$. The
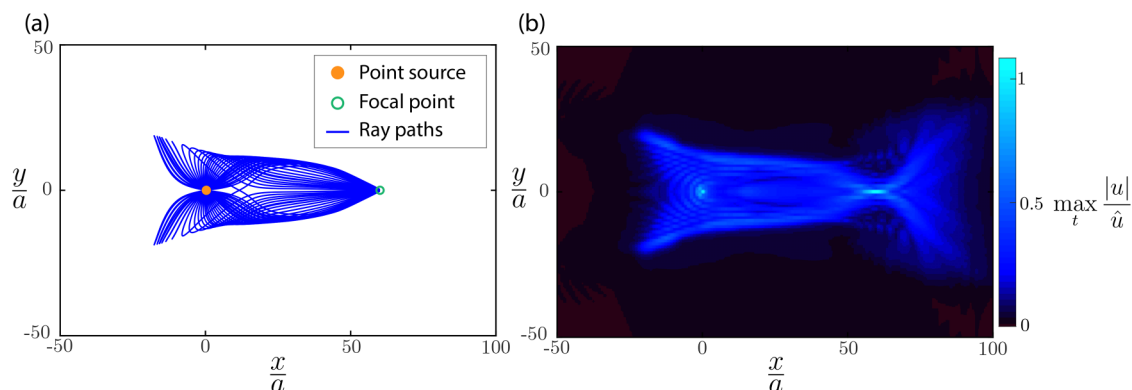

FIG. 6. Solutions for the point source focusing example. (a) Ray trajectories in the optimized lattice. (b) Maximum displacements during a transient numerical simulation in the optimized lattice.
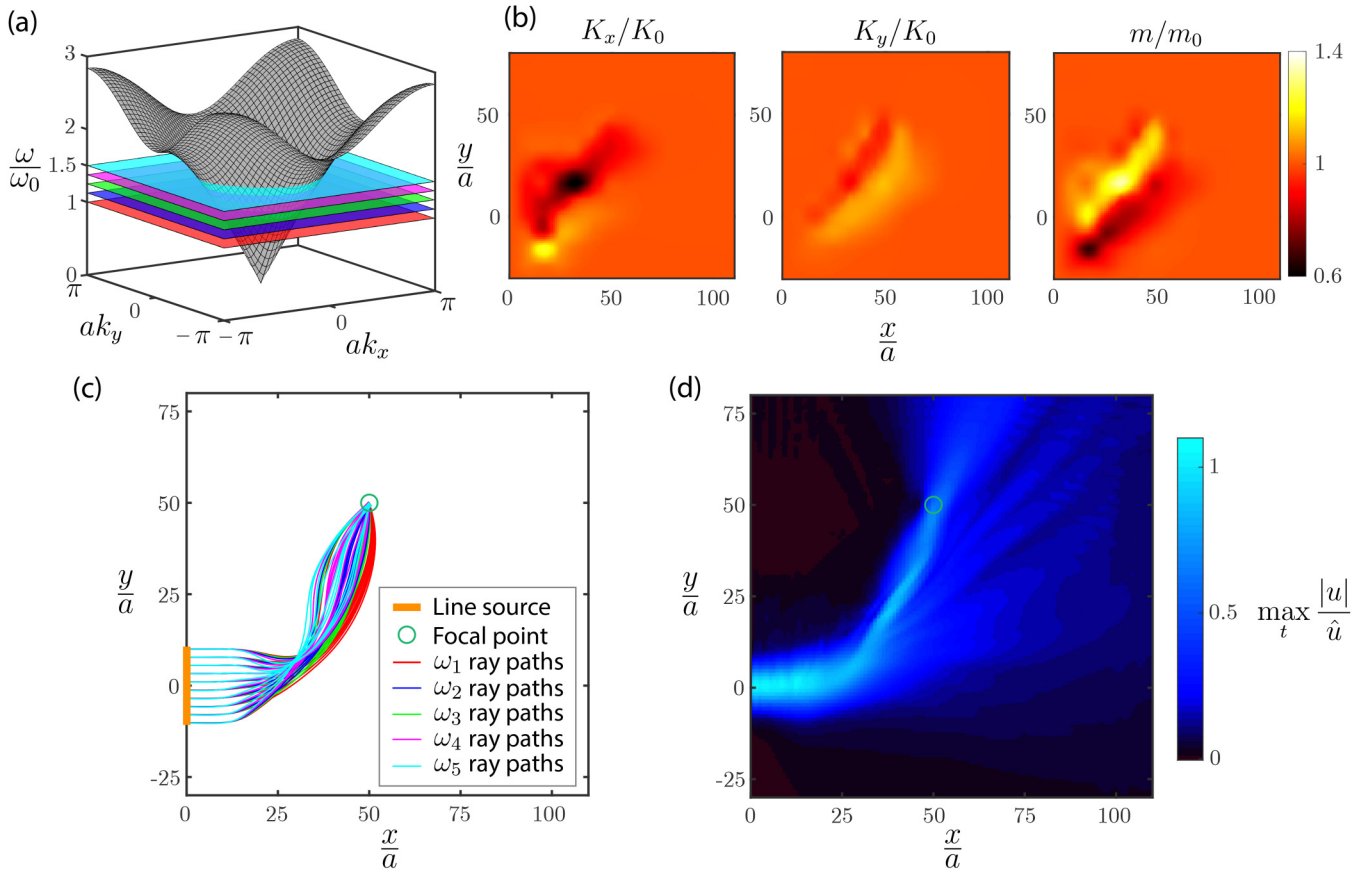
FIG. 7. Broadband focusing example. (a) Local dispersion relation at the line source, with the design frequencies highlighted. (b) Optimal design variable distributions. (c) Ray trajectories for the optimal design. (d) Maximum displacements during a transient numerical simulation for the optimal design.

simulation is carried out by numerically integrating the equation of motion of a finite grid until time $t = 415/\omega_0$. A sufficiently large domain was considered so that the wave does not reflect off domain boundaries. The maximum amplitude at each point during the simulation is plotted in Fig. 7(d). Additionally, Supplemental Video 2 animates the simulation.

The focusing effect is captured in the transient simulation, as high amplitudes are steered to the target focal point following the ray trajectories. A maximum amplitude of $u = 0.63\hat{u}$ is observed at the focal point. Simulations show some wave propagation outside of the region of the ray trajectories. This occurs primarily because the line source in the transient simulation does not purely excite a plane wave; it is impossible to avoid exciting wave vectors and frequency content not associated with the intended plane wave. Despite this, the desired behavior is clearly captured in the transient simulation.
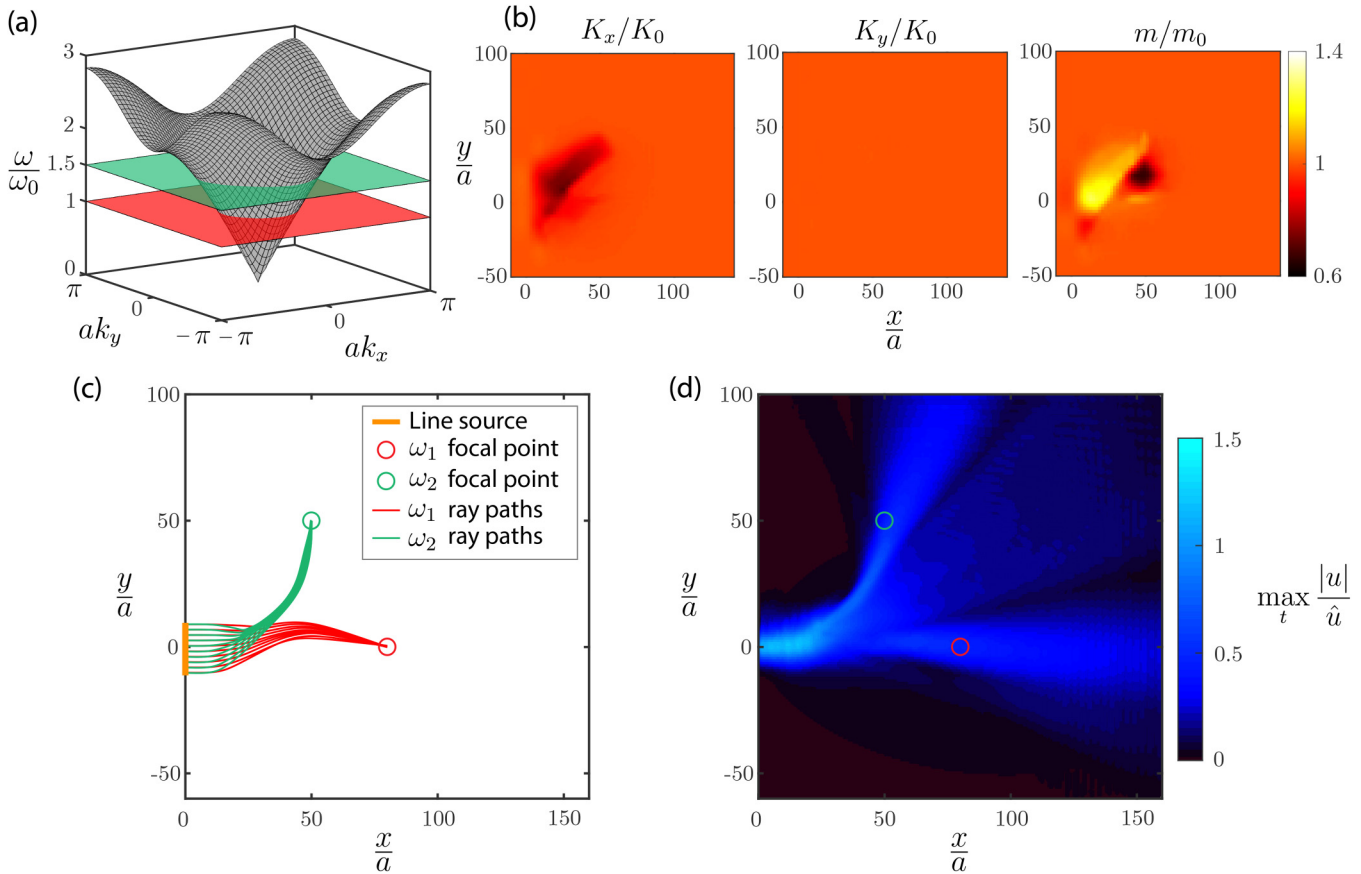
C. Frequency sorting

As a final example, we steer two frequencies of an incident plane wave to two different focal points. Again, we consider a line

source along the y-axis from $y = -10a$ to $y = 10a$. The objective is to steer rays of frequency $\omega_1 = \omega_0$ through the point $\hat{x}_1 = (80a, 0)^T$ and rays of frequency $\omega_2 = 1.5\omega_0$ through $\hat{x}_2 = (50a, 50a)^T$. The corresponding cost function takes the form

$$c_r = \begin{cases} \varphi_r^{*2}, & r \in I_1, \\ (\varphi_r^* - \hat{\varphi}_2)^2, & r \in I_2, \end{cases} \tag{23}$$

where I_1 indexes the set of ω_1-rays and I_2 indexes the set of ω_2-rays, and x_r^* is the point along ray r that first crosses the radial coordinate of its target focal point. The target frequencies are highlighted alongside the dispersion surface in Fig. 8(a).

For each frequency, 20 rays are included in the cost function, with equally spaced initial conditions along the line source. Unit cells in the region $x \leq 0$ are fixed with $K_x = K_y = K_0$ and $m = m_0$, while unit cells at $x > 0$ are being optimized, beginning from an initial guess of uniform mass and stiffness. The regularization constant is taken to be $\kappa = 0.001$.

15 November 2023 11:47:10

FIG. 8. Frequency sorting example. (a) Local dispersion relation at the line source, with the design frequencies $\omega_1 = \omega_0$ and $\omega_2 = 1.5\omega_0$ highlighted. (b) Optimal design variable distributions. (c) Ray trajectories for the optimal design. (d) Maximum displacements during a transient numerical simulation for the optimal design.

The optimal design variable distributions are plotted in Fig. 8(b), which range from 0.67 to 1.27 (the same bounds on the normalized design variables, from 0.2 to 2, are again applied, but the optimal solution did not reach the bounds). Again, only two design variables exhibit spatial grading, while K_y is nearly uniform. The optimal ray trajectories are shown in Fig. 8(c), where the two frequencies emerging from the line source are steered toward their respective focal points. Note that, while in the previous example we focused all considered frequencies at the same point, we here show that different focal points can also be achieved (and the frequencies considered here were included in the previous example).

A transient simulation was performed on a finite domain with the optimal mass and stiffness distributions. A line source excitation was applied to approximate an incident plane wave. Harmonic displacements of the form $u(y, t) = A(y)(\sin \omega_1 t + \sin \omega_2 t)$ were prescribed for all masses on the y-axis with the same amplitude profile $A(y)$ as for the previous example. The simulation was carried out until time $t = 415/\omega_0$, and the maximum displacement amplitude throughout the mass-spring network is reported in Fig. 8(d). Supplementary Video 3 shows an animation of the simulation.

The transient simulation shows the splitting of the incident plane wave into two beams. While frequency splitting is achieved, the focusing effect is not as clear as in the previous examples. At $\hat{x}_1$ and $\hat{x}_2$, maximum displacement amplitudes of $0.46\hat{u}$ and $0.45\hat{u}$ are observed, respectively. Displacement signals at the two target focal points are plotted in Fig. 9 in the time and frequency domains [where $|\tilde{u}(\omega)|$ denotes the amplitude of the fast Fourier transform of $u(t)$]. The frequency spectra show that each beam has the expected dominant frequency, though the two frequencies are not perfectly isolated. Again, the discrepancy between ray tracing and the transient simulation is largely due to the fact that the line source in the transient simulation does not excite a pure plane wave and there are other wave vectors present, which are not accounted for in the ray tracing.

D. Limitations

While the proposed inverse design framework is a flexible tool that enables exploration of the general design space of spatial grading, it is important to address its limitations. The optimization
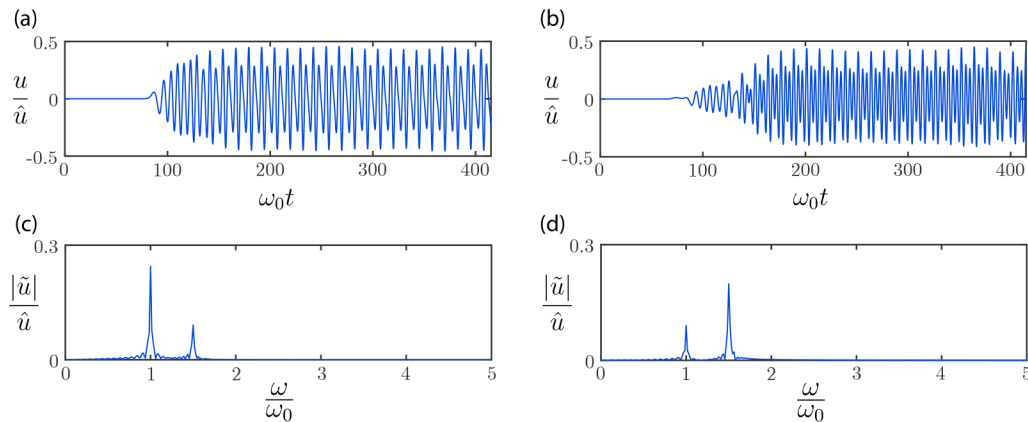
FIG. 9. Displacements at the target foci for the frequency sorting example, obtained from the transient simulation in Fig. 8(d). Time series displacement response at (a) the ω_1 focal point and (b) the ω_2 focal point. Frequency spectra of the displacements at (c) the ω_1 focal point and (d) the ω_2 focal point.

problems that arise are highly non-convex, and it is possible for the solver to identify undesirable local minima (and it may be unclear if better minima exist). Specifically, we found our implementation to find undesirable local minima, especially when operating in frequencies near the stopband. In such cases, a local stopband region may appear during the optimization, forcing the rays to sharply turn around to avoid this region, resulting in "tangled" rays, which can be difficult to recover from during numerical optimization. To address this limitation, alternative regularization techniques may be beneficial to penalize fast changes in ray trajectories.

Additionally, one must be cautious regarding the validity of ray theory and the underlying approximation of local periodicity. While in many cases, ray tracing provides an excellent approximation of the solution, for sufficiently fast spatial grading the assumptions will break down. Transient simulations can always be performed for validation of specific designs, but it remains an open problem to derive a practical validity condition for the ray approximation in phononic media (beyond the vague requirement that the spatial grading length scale is much larger than the wavelength). Furthermore, our ray formulation[19] does not capture waves propagating at frequencies within stopbands, which have complex wave vectors that lead to decaying amplitude. Waves propagating within a bandgap decay quickly, so it is reasonable to neglect them, as we are interested in guiding and focusing waves within passbands. However, future work can investigate the generalization of complex ray tracing formulations, e.g., from seismology,[20] which capture wave propagation in dissipative media, to phononic materials.

Finally, the mass-spring network has analytical dispersion relations. This allows for the required first and second derivatives of the dispersion relation to easily be obtained, which appear in the ray tracing Eqs. (1) and (2), the backward tracing Eqs. (16) and (17), and the cost function gradient of (20). More complicated media do not have analytical dispersion relations available (e.g., if the springs are replaced with beams[19]). In such cases, numerical calculation of the dispersion relation and its derivatives is required.

V. CONCLUSION

Spatially graded phononic materials offer control over wave propagation beyond what is possible with periodic architectures. While past research (in the short wavelength/high frequency regime) has primarily relied on simple spatial gradings and intuitive design, we present a systematic tool for the exploration of the immense design space of spatial grading. To overcome the bottleneck of computational efficiency, we leverage ray tracing to solve the forward problem. An optimization framework has been developed for the inverse design, which relies on the adjoint state method to obtain the cost function gradient.

We have demonstrated this inverse design framework on a two-dimensional mass-spring network, where the spatial distribution of mass and stiffness is computed to optimize various objectives. Specifically, we designed gradings that achieve focusing of an entire point source, broadband focusing of a plane wave, and guiding two different frequencies of a plane wave to different locations. These results demonstrate only a few of the exciting opportunities enabled by spatial grading. Additionally, the importance of accounting for the full dispersion relations in graded phononic media is made evident, which is not captured by transformation elastodynamics that relies on homogenized material properties.

Due to the generality and flexibility of this inverse design methodology, there are many opportunities for future research as cost functions can be formulated for a wide variety of problems (such as the design of caustic patterns or high-frequency cloaking). Moreover, our formulation in terms of an arbitrary dispersion relation is valid in any context where ray theory is valid. Beyond phononics, this includes the design of spatial gradings for the control of dispersive waves, e.g., in photonic crystals.[35–37]

SUPPLEMENTARY MATERIAL

Supplementary video 1 shows an animation of the transient numerical simulation for the point source focusing example of Fig. 6. Supplementary video 2 shows an animation of the transient

numerical simulation for the broadband focusing example of Fig. 7. Supplementary video 3 shows an animation of the transient numerical simulation for the frequency sorting example of Fig. 8.

ACKNOWLEDGMENTS

AUTHOR DECLARATIONS
Conflict of Interest

The authors have no conflicts to disclose.

Author Contributions

Charles Dorn: Conceptualization (equal); Data curation (lead); Formal analysis (lead); Funding acquisition (lead); Investigation (equal); Methodology (lead); Software (lead); Validation (lead); Visualization (lead); Writing – original draft (lead); Writing – review & editing (equal). **Dennis M. Kochmann:** Conceptualization (equal); Funding acquisition (supporting); Investigation (equal); Supervision (lead); Writing – review & editing (equal).

DATA AVAILABILITY

The data that support the findings of this study are available from the corresponding author upon reasonable request.

APPENDIX A: DERIVATION OF THE ADJOINT SYSTEM

With some manipulation, the adjoint Eq. (10) yields a system of first-order differential equations that is solvable along a ray. Here, we consider stationarity with respect to x and k separately. Stationarity with respect to x yields

$$\delta_{x}\mathscr{L} = \left(\frac{\partial C}{\partial x^{*}} - \rho\frac{\partial \mathscr{G}}{\partial x^{*}}\right)\delta x^{*} - \int_{0}^{t^{*}}\lambda^{\top}\left(\delta\dot{x} - \frac{\partial^{2}\omega}{\partial k\partial x}\delta x\right)dt - \int_{0}^{t^{*}}\mu^{\top}\frac{\partial^{2}\omega}{\partial x\partial x}\delta x\,dt = 0. \tag{A1}$$

Integrating by parts, the $\delta\dot{x}$-term in time leads to

$$\left(\frac{\partial C}{\partial x^{*}} - \rho\frac{\partial \mathscr{G}}{\partial x^{*}}\right)\delta x^{*} - \lambda^{\top}\delta x\big|_{0}^{t^{*}}$$
$$- \int_{0}^{t^{*}}\left(-\dot{\lambda} - \lambda^{\top}\frac{\partial^{2}\omega}{\partial k\partial x} + \mu^{\top}\frac{\partial^{2}\omega}{\partial x\partial x}\right)\delta x\,dt = 0. \tag{A2}$$

Since the initial conditions are fixed, $\delta x|_{t=0} = \mathbf{0}$. This must hold for an arbitrary δx, so we obtain a first-order differential equation

for λ and μ along with an end condition at t^{*},

$$\dot{\lambda} = -\frac{\partial^{2}\omega}{\partial x\partial k}\lambda + \frac{\partial^{2}\omega}{\partial x\partial x}\mu, \quad t \in [0, t^{*}],$$
$$\lambda(t^{*}) = \frac{\partial C}{\partial x^{*}} - \rho\frac{\partial \mathscr{G}}{\partial x^{*}}. \tag{A3}$$

A similar analysis is performed for stationarity with respect to k, beginning with the stationarity condition

$$\delta_{k}\mathscr{L} = -\int_{0}^{t^{*}} -\lambda^{\top}\frac{\partial^{2}\omega}{\partial k\partial k}\delta k\,dt - \int_{0}^{t^{*}}\mu^{\top}\left(\dot{\delta k} + \frac{\partial^{2}\omega}{\partial x\partial k}\delta k\right)dt = 0. \tag{A4}$$

Integration by parts gives

$$-\mu^{\top}\delta k\big|_{0}^{t^{*}} - \int_{0}^{t^{*}}\left(-\lambda^{\top}\frac{\partial^{2}\omega}{\partial k\partial k} + \mu^{\top}\frac{\partial^{2}\omega}{\partial x\partial k} - \dot{\mu}\right)\delta k\,dt = 0. \tag{A5}$$

The fixed initial conditions of the ray require that $\delta k|_{t=0} = \mathbf{0}$. Since this must hold for arbitrary δk, we obtain

$$\dot{\mu} = -\frac{\partial\omega^{2}}{\partial k\partial k}\lambda + \frac{\partial^{2}\omega}{\partial k\partial x}\mu, \quad t \in [0, t^{*}],$$
$$\mu(t^{*}) = \mathbf{0}. \tag{A6}$$

We consider cost functions independent of k, but one can include k-dependence in the cost function, which leads to a nonzero end condition for μ.

Equations (A3) and (A6) represent the adjoint system, with end conditions defined at $t = t^{*}$. This can be solved as a final value problem, starting at t^{*} and marching backward in time along the ray trajectory to $t = 0$.

APPENDIX B: DISPERSION RELATION DERIVATIVES

The first and second derivatives of the dispersion relation are required in the ray tracing system, Eqs. (1) and (2), the adjoint system, Eqs. (16) and (17), and in the cost function gradient computation, Eq. (20). Here, we define these derivatives.

In our implementation, each design variable $\theta^{(i)}$ is defined on a discrete uniform $n \times n$ grid. To obtain spatial derivatives of the dispersion relation at arbitrary locations away from the grid points, we employ bicubic interpolation. Using bicubic interpolation ensures continuous spatial derivatives, which we found led to better performance than bilinear interpolation that has discontinuous spatial derivatives.

The design variable field $\tilde{\theta}^{(i)}(x, \theta^{(i)}): \mathbb{R}^{d} \times \mathbb{R}^{n^{2}} \to \mathbb{R}$ interpolates the design parameter at grid points to an arbitrary point x. The local dispersion relations vary smoothly in space, dependent on the design variables only through the interpolated quantity, i.e., $\omega(k, x, \theta) = \tilde{\omega}(k, \tilde{\theta}(x, \theta))$. For example, in the mass-spring network, the local dispersion relations of Eq. (4) depend directly on the values of the design variables K_{x}, K_{y}, and m at an arbitrary point x, obtained by the bicubic interpolating of the mass and stiffness at the grid points.

15 November 2023 11:47:10

Given this dependence, the dispersion relation derivatives appearing in the adjoint system and cost function gradient relation take the form

$$\frac{\partial \omega}{\partial x_p} = \sum_{i=1}^{D} \frac{\partial \tilde{\omega}}{\partial \tilde{\theta}^{(i)}} \frac{\partial \tilde{\theta}^{(i)}}{\partial x_p},$$

$$\frac{\partial^2 \omega}{\partial x_p \partial x_q} = \sum_{i=1}^{D} \sum_{j=1}^{D} \left(\frac{\partial \tilde{\theta}^{(j)}}{\partial x_q} \frac{\partial^2 \tilde{\omega}}{\partial \tilde{\theta}^{(j)} \partial \tilde{\theta}^{(i)}} \frac{\partial \tilde{\theta}^{(i)}}{\partial x_p} + \frac{\partial \tilde{\omega}}{\partial \tilde{\theta}^{(i)}} \frac{\partial^2 \tilde{\theta}^{(i)}}{\partial x_p \partial x_q} \right),$$

(B1)

$$\frac{\partial^2 \omega}{\partial x_p \partial k_s} = \sum_{i=1}^{D} \frac{\partial^2 \tilde{\omega}}{\partial \tilde{\theta}^{(i)} \partial k_s} \frac{\partial \tilde{\theta}^{(i)}}{\partial x_p},$$

$$\frac{\partial^2 \omega}{\partial x_p \partial \theta_l^{(j)}} = \sum_{i=1}^{D} \left(\frac{\partial \tilde{\theta}^{(j)}}{\partial \theta_l^{(j)}} \frac{\partial^2 \tilde{\omega}}{\partial \tilde{\theta}^{(j)} \partial \tilde{\theta}^{(i)}} \frac{\partial \tilde{\theta}^{(i)}}{\partial x_p} + \frac{\partial \tilde{\omega}}{\partial \tilde{\theta}^{(i)}} \frac{\partial^2 \tilde{\theta}^{(i)}}{\partial x_p \partial \theta_l^{(j)}} \right),$$

(B2)

$$\frac{\partial^2 \omega}{\partial k_s \partial \theta_l^{(i)}} = \frac{\partial^2 \tilde{\omega}}{\partial k_s \partial \tilde{\theta}^{(i)}} \frac{\partial \tilde{\theta}^{(i)}}{\partial \theta_l^{(i)}}.$$

(B3)

The derivatives of $\tilde{\theta}$ with respect to $\boldsymbol{x}$ and $\boldsymbol{\theta}$ are evaluated using the interpolation functions and design variables at surrounding grid points.

For the mass-spring network, the derivatives of the dispersion relations with respect to $\tilde{\theta}$ and $\boldsymbol{k}$ are available by analytically differentiating Eq. (4) (recalling that $\tilde{\theta}^{(1)} = K_x$, $\tilde{\theta}^{(2)} = K_y$, and $\tilde{\theta}^{(3)} = m$).

REFERENCES

[1]M. I. Hussein, M. J. Leamy, and M. Ruzzene, "Dynamics of phononic materials and structures: Historical origins, recent progress, and future outlook," Appl. Mech. Rev. **66**, 040802 (2014).
[2]O. Sigmund and J. Søndergaard Jensen, "Systematic design of phononic band–gap materials and structures by topology optimization," Philos. Trans. R. Soc. London. Ser. A **361**, 1001–1019 (2003).
[3]O. R. Bilal and M. I. Hussein, "Ultrawide phononic band gap for combined in-plane and out-of-plane waves," Phys. Rev. E **84**, 065701 (2011).
[4]G. Yi and B. D. Youn, "A comprehensive survey on topology optimization of phononic crystals," Struct. Multidiscipl. Optim. **54**, 1315–1344 (2016).
[5]G. Trainiti, J. J. Rimoli, and M. Ruzzene, "Wave propagation in undulated structural lattices," Int. J. Solids Struct. **97**, 431–444 (2016).
[6]G. Trainiti, J. J. Rimoli, and M. Ruzzene, "Optical evaluation of the wave filtering properties of graded undulated lattices," J. Appl. Phys. **123**, 091706 (2018).
[7]J. M. De Ponti, *Graded Elastic Metamaterials for Energy Harvesting* (Springer, 2021).
[8]L. Zhao, C. Bi, H. Huang, Q. Liu, and Z. Tian, "A review of acoustic Luneburg lens: Physics and applications," Mech. Syst. Signal Process. **199**, 110468 (2023).
[9]S.-C. S. Lin, T. J. Huang, J.-H. Sun, and T.-T. Wu, "Gradient-index phononic crystals," Phys. Rev. B **79**, 094302 (2009).
[10]S. Tol, F. L. Degertekin, and A. Erturk, "Gradient-index phononic crystal lens-based enhancement of elastic wave energy harvesting," Appl. Phys. Lett. **109**, 063902 (2016).
[11]C. Dorn and D. M. Kochmann, "Conformally graded metamaterials for elastic wave guidance," Extreme Mech. Lett. **65**, 102091 (2023).

[12]J. Zhu, Y. Chen, X. Zhu, F. J. Garcia-Vidal, X. Yin, W. Zhang, and X. Zhang, "Acoustic rainbow trapping," Sci. Rep. **3**, 1728 (2013).
[13]S. Tol, F. L. Degertekin, and A. Erturk, "Phononic crystal Luneburg lens for omnidirectional elastic wave focusing and energy harvesting," Appl. Phys. Lett. **111**, 013503 (2017).
[14]H. Chen and C. T. Chan, "Acoustic cloaking and transformation acoustics," J. Phys. D: Appl. Phys. **43**, 113001 (2010).
[15]Z. Sun, X. Sun, H. Jia, Y. Bi, and J. Yang, "Quasi-isotropic underwater acoustic carpet cloak based on latticed pentamode metafluid," Appl. Phys. Lett. **114**, 094101 (2019).
[16]Z. Chang and G. Hu, "Elastic wave omnidirectional absorbers designed by transformation method," Appl. Phys. Lett. **101**, 054102 (2012).
[17]Y. Chen, J. Hu, and G. Huang, "A design of active elastic metamaterials for control of flexural waves using the transformation method," J. Intell. Mater. Syst. Struct. **27**, 1337–1347 (2016).
[18]H. Nassar, Y. Chen, and G. Huang, "Polar metamaterials: A new outlook on resonance for cloaking applications," Phys. Rev. Lett. **124**, 084301 (2020).
[19]C. Dorn and D. M. Kochmann, "Ray theory for elastic wave propagation in graded metamaterials," J. Mech. Phys. Solids **168**, 105049 (2022).
[20]V. Cervenỳ, *Seismic Ray Theory* (Cambridge University Press, Cambridge, 2001), Vol. 110.
[21]D. Malacara-Hernández and Z. Malacara-Hernández, *Handbook of Optical Design* (CRC Press, 2017).
[22]D. C. O'Shea, *Elements of Modern Optical Design* (Wiley, New York, 1985), Vol. 2.
[23]T.-W. Lo and P. L. Inderwiesen, *Fundamentals of Seismic Tomography* (Society of Exploration Geophysicists, 1994).
[24]A. Authier, "Dynamical theory of x-ray diffraction," in *International Tables for Crystallography* (Oxford University Press, 2006), pp. 534–551.
[25]A. Teh, M. O'Toole, and I. Gkioulekas, "Adjoint nonlinear ray tracing," ACM Trans. Graph. **41**, 1–13 (2022).
[26]R. S. Langley, "The response of two-dimensional periodic structures to point harmonic forcing," J. Sound Vib. **197**, 447–469 (1996).
[27]N. Rawlinson, S. Pozgay, and S. Fishwick, "Seismic tomography: A window into deep Earth," Phys. Earth Planet. Inter. **178**, 101–135 (2010).
[28]D. Givoli, "A tutorial on the adjoint method for inverse problems," Comput. Methods Appl. Mech. Eng. **380**, 113810 (2021).
[29]G. Chavent, "Identification of functional parameters in partial differential equations," in *Joint Automatic Control Conference* (American Society of Mechanical Engineers, 1974), Vol. 12, pp. 155–156.
[30]R.-E. Plessix, "A review of the adjoint-state method for computing the gradient of a functional with geophysical applications," Geophys. J. Int. **167**, 495–503 (2006).
[31]T. W. Hughes, M. Minkov, I. A. Williamson, and S. Fan, "Adjoint method and inverse design for nonlinear nanophotonic devices," ACS Photonics **5**, 4781–4787 (2018).
[32]J. L. Lions, *Optimal Control of Systems Governed by Partial Differential Equations* (Springer, 1971), Vol. 170.
[33]D. C. Liu and J. Nocedal, "On the limited memory BFGS method for large scale optimization," Math. Program. **45**, 503–528 (1989).
[34]S. G. Johnson, see https://github.com/stevengj/nlopt for "The NLopt nonlinear-optimization package" (2007).
[35]P. S. J. Russell and T. Birks, "Hamiltonian optics of nonuniform photonic crystals," J. Lightwave Technol. **17**, 1982 (1999).
[36]Y. Jiao, S. Fan, and D. A. Miller, "Designing for beam propagation in periodic and nonperiodic photonic nanostructures: Extended Hamiltonian method," Phys. Rev. E **70**, 036612 (2004).
[37]E. Cassan, K.-V. Do, C. Caer, D. Marris-Morini, and L. Vivien, "Short-wavelength light propagation in graded photonic crystals," J. Lightwave Technol. **29**, 1937–1943 (2011).